J. Fluid Mech. (1991), *vol.* 224, *pp.* 91–115
Printed in Great Britain

The response of microscopic bubbles to sudden changes in the ambient pressure

By BING RAN AND JOSEPH KATZ
Department of Mechanical Engineering, The Johns Hopkins University, Baltimore, MD 21218, USA

(Received 28 March 1990 and in revised form 24 July 1990)

This paper focuses on the response of bubbles to sudden changes in the ambient pressure. Trains of bubbles with radii varying between 45 and 200 μm were exposed to various pressure steps, and their response was monitored by pulsed laser holography. The experiments were performed in a specially constructed chamber, allowing generation of pressure steps ranging from 0.1 to 20 times the initial value. Air, CO_2, helium and hydrogen bubbles were selected, providing a range of mass, thermal diffusivities, solubilities in water and isentropic constants. The changes in the bubbles' diameters were determined by reconstructing the holograms, magnifying the images and measuring the sizes of individual bubbles. Most of the experiments were performed with pressure changes at the rate of 20 KPa/ms, and most data were recorded in less than 20 ms. The results confirm that, within the present range of test conditions, the bubbles can respond instantaneously to changes in the ambient pressure. The experiments also demonstrate that the response of the bubbles at the present timescales can be assumed to be isothermal (polytropic constant of 1.0), irrespective of the bubble content or size. Repeated measurements with different pressure waveforms, but with the same final pressure resulted in identical results, demonstrating that bubbles can be used as pressure sensors. Variations in timescales up to a few hundred milliseconds still resulted in the same response, confirming the isothermal assumption. The dissolved gas content had a noticeable effect on the behaviour of the CO_2 bubbles, the most soluble of the gases tested, and had no detectable effect on the behaviour of air bubbles. The paper also includes a detailed error evaluation of the present experiments and an estimate of the expected error when the bubbles are utilized as pressure sensors.

1. Introduction

1.1. *Background*

The response of bubbles to changes in the ambient pressure has been a subject of numerous studies over the years. Several review papers, such as Plesset & Prosperetti (1977), and Arndt (1981) provide extensive summaries, the former on bubble dynamics, and the latter on cavitation. The primary interest has been among cavitation researchers, who tried to predict the behaviour of microscopic free-stream bubbles as they develop to large-scale visible cavitation. The idea of utilizing microscopic bubbles as pressure sensors was introduced first by Ooi & Acosta (1983) while attempting to resolve the pressure fluctuations within water jets. They assumed a quasi-steady response of bubbles, namely that they were at equilibrium at any time with their environment. They based their assumption on a comparison

between the characteristic spectra of pressure and velocity fluctuations within jets (Fuchs 1972 and Hussain 1986 are examples of the numerous sources of information) and the resonant frequencies of 100 μm diameter bubbles (to be discussed shortly). They still had to assume a relationship between the pressure and the density of the gas within the bubble (a polytropic constant), in order to relate the bubble size to the ambient pressure. Similar experiments in a two-dimensional shear layer were performed by O'Hern (1987), and within a tip vortex by Green (1988). Both demonstrated the larger variations in the results depending on the chosen values for the polytropic constants. Determination of this constant, and its dependence on various flow parameters are some of the objectives of the present study.

A theoretical analysis leading to the appropriate choice of polytropic constants was performed by Prosperetti (1977, 1984) and these were measured in sound fields by Crum (1983). The experimentally observed trends agreed with the theoretical values, but the actual data were scattered over a considerable range. Based on Prosperetti's criteria the pressure–density relationship for the bubbles used by Ooi & Acosta (1983) could be assumed to be isothermal for most of the pressure fluctuation spectra in water jets. Recently, Prosperetti, Crum & Commander (1988) raised some questions about the use of polytropic constants. Instead, they performed direct computations of the equations of momentum and energy within the bubble. Their analysis neglected the effect of mass diffusion and assumed that there are no spatial variations in the bubble's internal pressure (unlike the density and temperature). Their analysis also includes a comparison between the two computation techniques (polytropic constant *vs.* direct computations). They conclude that significant differences occur when the excitation frequency is at the same order as the bubble's resonant frequency (the primary differences occur at ω/ω_0 of about 0.8 and 0.45, depending on the bubble size). As will be shown shortly, the natural frequency of a 100 μm diameter bubble is about 55 KHz. Thus, the results of Prosperetti *et al.* suggest that one cannot utilize the polytropic-constant approach for measuring pressure fluctuations with frequencies exceeding 20 KHz. The value of this constant at lower frequencies is an important part of this project. However, it requires a brief theoretical background in bubble dynamics which is summarized in the following section.

1.2. *Theoretical background*

The response of a single bubble in an infinite, incompressible liquid medium is described by the Rayleigh–Plesset equation:

$$R\ddot{R}+\tfrac{3}{2}\dot{R}^2=\frac{1}{\rho}\left[P_{\mathrm{v}}-P_{\infty}-\frac{4\mu\dot{R}}{R}-\frac{2\sigma}{R}+P_{\mathrm{g}}\right]. \tag{1}$$

Here R is the bubble radius, $\dot{R}$ and $\ddot{R}$ are its first and second time derivatives (velocity and acceleration), respectively, σ is the surface tension, ρ and μ are the liquid's density and viscosity, respectively, P_{∞} is the ambient pressure, and P_{g} and P_{v} are the partial pressures of gas and liquid vapour, respectively. A modified version of this equation that brings the liquid compressibility into consideration was developed by Keller & Miksis (1980). However, since the present project does not deal with velocities comparable with the speed of sound in liquid, the compressibility effects are insignificant. At equilibrium $\dot{R}$ and $\ddot{R}$ are zero and the pressure–radius relationship becomes

$$P_{\mathrm{v}}-\frac{2\sigma}{R_0}+P_{\mathrm{g0}}=P_{\infty}. \tag{2}$$

The subscript 0 indicates initial or equilibrium conditions. P_g is unknown and usually depends on the density and temperature of gas within the bubble. Assuming a polytropic pressure–density relationship in the form of

$$\frac{P_g}{\rho_g^k} = \text{constant} \tag{3}$$

(ρ_g is the gas density and k is the polytropic constant), and that the mass of gas within the bubble remains constant leads to the following pressure–radius relationship:

$$P_g = P_{g0}\left(\frac{R_0}{R}\right)^{3k}. \tag{4}$$

The response of a bubble to small perturbations in the ambient pressure can be estimated by assuming a radius variation in the form

$$R = R_0(1+\epsilon e^{i\omega t}), \tag{5}$$

where $\epsilon \ll 1$. By substituting this expression into the Rayleigh–Plesset equation and keeping only the first-order terms one can obtain a quadratic expression for ω:

$$\omega^2 - \frac{4\nu i}{R_0^2}\omega + \frac{2\sigma}{\rho R_0^3} - \frac{3P_{g0}}{\rho R_0^2} = 0 \tag{6}$$

with a solution

$$\omega = \frac{2\nu i}{R_0^2} \pm \left[-\frac{4\nu^2}{R_0^4} - \frac{2\sigma}{\rho R_0^3} + \frac{3P_{g0}}{\rho R_0^2}\right]^{\frac{1}{2}}. \tag{7}$$

The imaginary part of this equation represents viscous damping, and in its absence one can obtain the well-known expression for the bubble's natural frequency, ω_0:

$$\omega_0 = \left[\frac{3P_{g0}}{\rho R_0^2} - \frac{2\sigma}{\rho R_0^3}\right]^{\frac{1}{2}}. \tag{8}$$

By replacing P_{g0} with $P_\infty - P_v + 2\sigma/R_0$ the expression for the natural frequency becomes

$$\omega_0 = \left[\frac{3}{\rho R_0^2}\left(P_\infty - P_v + \frac{4\sigma}{3R_0}\right)\right]^{\frac{1}{2}}. \tag{9}$$

Thus, an air bubble with an initial radius of 50 μm and atmospheric equilibrium gas pressure ($\sigma = 72 \times 10^{-3}$ N/m) has a natural frequency of 3.5×10^5 rad/s (55 KHz). Since ω_0 is inversely proportional to R one would like the pressure sensor to be as small as possible. As will be discussed later, a characteristic radius of 50 μm is a compromise between the desire to increase the bubble's natural frequency and the need to resolve small changes in the size of this 'pressure sensor'. The natural frequency of this bubble is still much higher than the typical frequencies of pressure fluctuations within turbulent flows. For example, according to Fuchs (1972), as well as Arndt & George (1978), the characteristic Strouhal number of peak pressure fluctuations, fD/U (f is the frequency, D is the jet diameter, and U is the velocity) is about 0.5. Thus, at a velocity of 20 m/s, and with a 2.5 cm diameter jet, the peak in the pressure fluctuation spectrum is at 360 Hz. Note that the Strouhal number refers to Eulerian pressure fluctuations, and the pressure sensed by the bubble is closer to Lagrangian fluctuations (the bubble still slips). The frequency of significant

fluctuations, however, extends to values about an order of magnitude higher, namely to about 4 KHz. This range is still an order of magnitude lower than the bubble's natural frequency. Thus, one should expect a 50 μm bubble to respond almost instantaneously to pressure fluctuations within the jet described above. As long as the frequency of pressure fluctuations is much lower than ω_0, the bubble behaviour can be considered to be 'quasi-steady', namely it is in dynamic equilibrium with its environment. The pressure–radius relation then becomes

$$P = P_{g0}\left(\frac{R_0}{R}\right)^{3k} + P_v - \frac{2\sigma}{R}. \tag{10}$$

What happens if ϵ is in the order of 1.0, but $\omega \ll \omega_0$? Then, from (5) the magnitudes of the terms on the right-hand side of (1) are

$$|R\ddot{R}| = \omega^2 \epsilon R_0^2, \quad |\dot{R}^2| = \omega^2 \epsilon^2 R_0^2. \tag{11}$$

For $\omega = 360$ Hz (2262 rad/s), and a 50 μm radius bubble both terms in (11) are equal to 0.013, still a very small number compared with each of the pressure terms on the right-hand side of (1). P_g/ρ and P_∞/ρ are of the order of 100, and $2\sigma/\rho R$ is equal to 2.9. Thus, as long as the frequency is low, and even for large changes in the size of the bubble, it still can be assumed to be in equilibrium with the ambient pressure. By substituting (2) into (10) the pressure–radius relationship becomes

$$P = \left(P_0 + \frac{2\sigma}{R_0} - P_{v0}\right)\left(\frac{R_0}{R}\right)^{3k} - \frac{2\sigma}{R} + P_v, \tag{12}$$

where the subscript 0 indicates the initial condition. This simple expression can be used for computing the pressure from the bubble radius, provided that P_{g0}, R_0, R and k are known. σ and P_v are functions of the temperature, and are assumed to be constant.

The value of k in (12) is still unknown and, as already mentioned, is one of the main objectives of the present research project. If the process is adiabatic, k is equal to the isentropic constant, namely 1.4 and 1.67 for diatomic and monoatomic gases, respectively. If a compression or expansion process is isothermal, the value of k is 1.0. Both the thermal diffusivity, α, of the gas within the bubble, and the timescales of the process affect the value of k. A slow process allows more time for heat transfer, and a higher thermal diffusivity results in higher rates of heat transfer. The more heat exchange that occurs between the bubble and its environment, the closer the process is to becoming isothermal. As noted before, Prosperetti (1977) computed the value of k for bubbles exposed to sound waves. Following a similar approach, but limiting the discussion to fluctuations up to the order of 10% of the bubble's natural frequency, one can define a thermal penetration distance of the order of $(\alpha/\omega)^{\frac{1}{2}}$, and compare its value to the bubble radius. If

$$\frac{R}{(\alpha/\omega)^{\frac{1}{2}}} < 1 \tag{13}$$

the process is more likely to be isothermal. For a 50 μm radius air bubble at atmospheric pressure, which is exposed to 4 KHz (25133 rad/s) fluctuations, the value of the expression in (13) is 0.67 (1.7 if the frequency is calculated at rad/s). Values for α are provided in table 1 below. Based on Prosperetti's (1977) analysis the bubble behaviour under these conditions should still be close to isothermal. We shall return to this issue following the presentation of the results.

Similarly to heat diffusion, mass diffusion is also involved since the entire analysis is based on the assumption that the mass of the bubble remains constant. However, since the mass diffusion coefficient, D, of air in water is very small (table 1), the value of $R/(D/\omega)^{\frac{1}{2}}$ is very large. Specifically, for the same bubble size and the same excitation frequency, the value of this parameter is 71, namely about two orders of magnitude larger than the thermal values. Thus, the assumption of negligible mass transfer seems to be reasonable. However, the concentration of dissolved gas compared to the saturation level also affects the rate of mass transfer, particularly for highly soluble gases such as CO_2 (see table 1). As a result, the assumption of negligible mass transfer should be tested by comparing, for example, the behaviour of CO_2 bubbles in supersaturated and highly undersaturated liquids. Experiments at similar pressures, but substantially different timescales can also identify significant changes in the mass of the bubble and, as a result, the role of mass diffusion. As will be shown later, the present experiments confirmed that mass diffusion was insignificant, at least for the operating conditions described in this paper.

It should be mentioned here that another phenomenon, which is usually referred to as 'rectified diffusion' (Hsieh & Plesset 1961), occurs when bubbles are exposed to an oscillating pressure field for extended periods of time. Owing to differences between the outflux of mass during the compression phase and the influx during expansion, there is a net change in the mass of the bubble during each cycle. This phenomenon is very slow (it takes about 10^5 s for a 200 μm bubble to double its size), and has a significant impact only after an extended exposure to pressure oscillations. For example, when a bubble is located near an underwater sound source it eventually grows owing to rectified diffusion. This phenomenon should not have any impact on the present experiments.

2. Experimental set-up and procedures

2.1. *Holography*

In principle the experiments consisted of injecting a train of bubbles with a constant known diameter (about 100 μm), exposing these bubbles to different pressures, and measuring the resulting size changes. As a result, the experiments had to include simultaneous measurements of the diameter of several moving microscopic bubbles. Recording a detailed image of numerous microscopic objects located randomly in space without loss of resolution required the use of holography. The process consisted of recording holograms of the desired sample volume with a high-power pulsed laser and reconstructing them. The observations and measurements were made within the reconstructed image by utilizing optics capable of magnifying portions of the field by about 500 times. Since the final objective of this project is to use these bubbles as pressure sensors in turbulent flows, the recording time of a single image has to be sufficiently short to prevent blurring of the image. A resolution in the order of 1 μm for an object moving at 20 m/s requires a maximum exposure time of 50 ns. This short exposure time, and the energy required for recording a hologram, limit the possible light sources to a high-power pulsed solid-state laser. Of them, the ruby laser with intra-cavity etalons is the most coherent (without using elaborate multi-component, inhibitively expensive set-ups), and as a result, the most useful for holography. The laser available to us can generate up to three 25 ns pulses and the delay between these pulses can be varied between 10 to 600 ms. Only one pulse was used during the calibration phase. We have opted to utilize the inline Frounhofer holography method, since it is particularly suitable for microscopic objects located

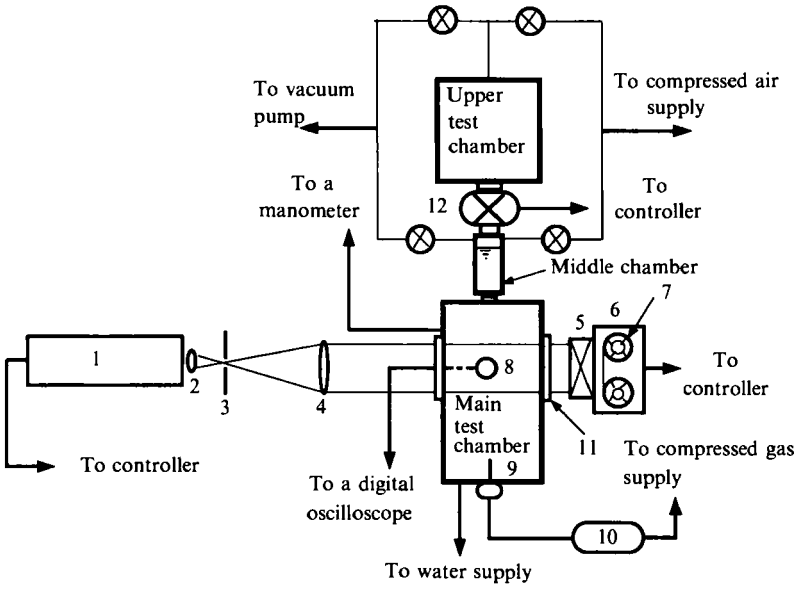

FIGURE 1. A schematic description of the calibration chamber and the inline holocamera. 1, Triple pulsed ruby laser; 2, microscope objective; 3, spatial filter; 4, collimating lens; 5, shutter; 6, automatic film drive; 7, holographic film; 8, piezoresistive and piezoelectric transducers; 9, bubble injector; 10, filter and fine metering valve; 11, replaceable windows; 12, fast opening valve.

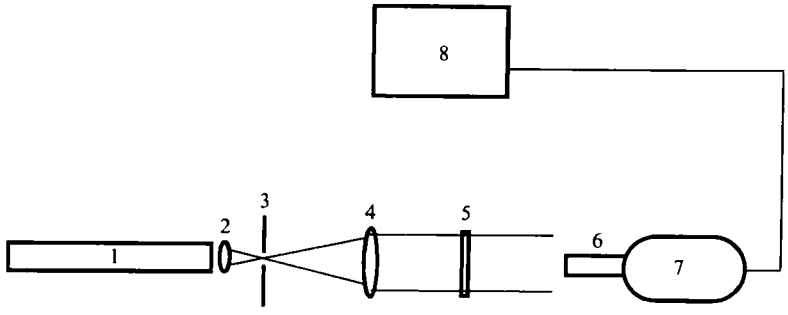

FIGURE 2. A schematic description of the reconstruction system. 1. He–Ne laser; 2, microscope objective; 3, spatial filter; 4, collimating lens; 5, hologram; 6, camera objective lens; 7, camera; 8, monitor.

in the far field of the film plane (see Collier, Burkhardt & Lin 1970 for further details). The optical set-up is included in figure 1, and the reconstruction system is sketched in figure 2. In this inline system the laser output is spatially filtered, expanded to 75 mm diameter, and collimated before illuminating the sample volume. Part of the light is diffracted by the objects in this volume and interferes with the undisturbed remainder of the beam. The resulting interference pattern is recorded on a high-resolution film (AGFA Gevaert 10E75).

After being developed the hologram is mounted on the reconstruction system, which uses a He-Ne laser as a light source. Observations are then made within the reconstructed image. Reconstruction with a He–Ne laser, which has a wavelength of 0.628 μm, as opposed to the ruby's 0.6943 μm, does not change the lateral magnification of the image (Collier *et al.* 1970). However, the axial distance expands

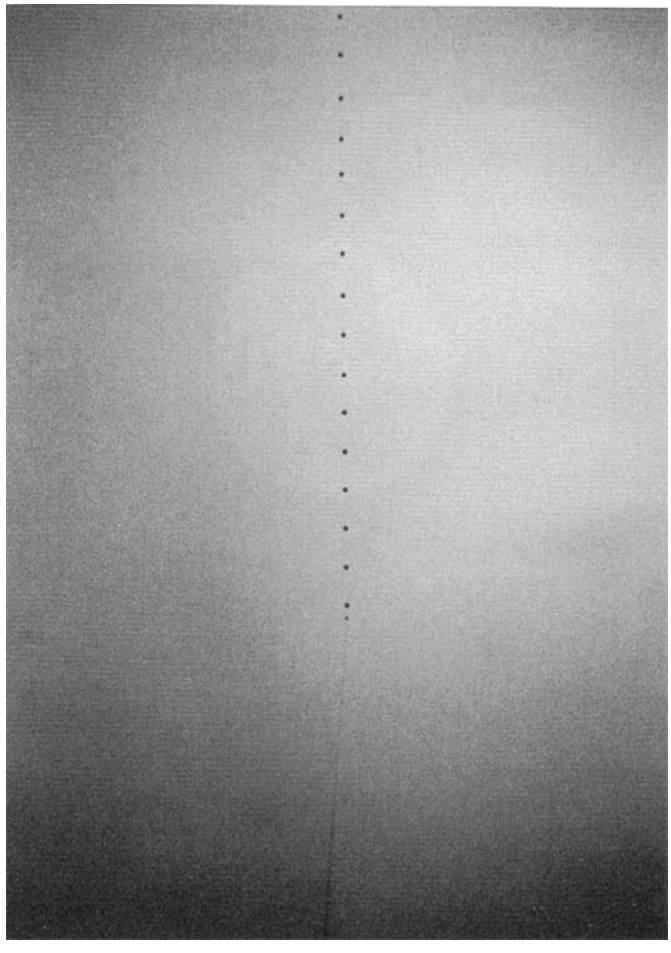

FIGURE 3. A photograph of a train of 150 μm diameter bubbles.

by a factor equal to the wavelength ratio, that is by 1.106. The exact magnification was determined during the experiments by recording holograms of microscope reticules. In most cases the entire TV monitor (figure 2) covered an area of about 600×500 μm.

2.2. *Test facility*

A special calibration chamber was constructed for the present series of experiments. A schematic description of this set-up is included in figure 1. The facility consists of three chambers, the bottom two permanently connected by several tubes, and the upper one separated by a fast-opening solenoid valve. The bottom chamber was the actual test section. It was made of thick Lexane walls and was surrounded by an aluminium safety frame. This chamber was 90 cm high and had a 15×15 cm rectangular cross-section. The upper two chambers were used solely for generating the pressure waves. The middle chamber was a 2 in. pipe, whereas the upper container was a 6 in. pipe. The two upper chambers were connected to sources of compressed air and to a vacuum pump. The water level was usually kept just below the top of the middle chamber, whereas the much larger upper chamber contained only air.

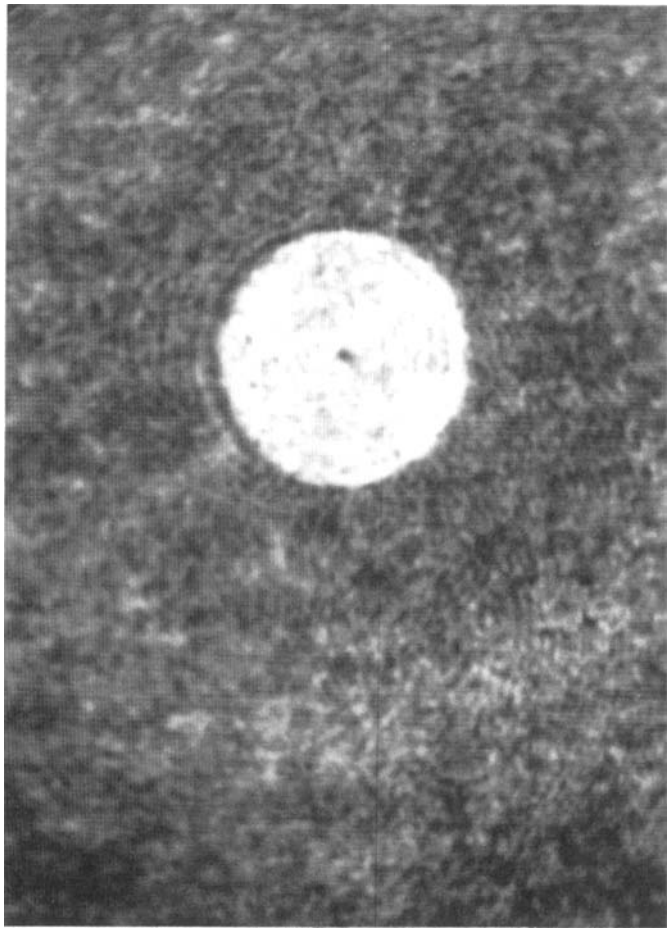

FIGURE 4. A typical reconstructed image of a 150 μm diameter bubble as it appears on the monitor screen.

During an experiment, different pressures were established in the middle and upper containers. At a prescribed time the solenoid valve was opened causing a sudden increase or reduction of pressure in the test section. Two pressure transducers, with piezoelectric (PCB model 102A05) and piezoresistive (Entran model EPN-3001-50A) sensors were installed on the walls of the main test section at the same elevation as the holocamera windows. They were calibrated regularly using a mercury manometer and against each other. For convenience, the data presented in this paper rely on the piezoresistive transducer, and on systematic comparison with the manometer's reading. Based on the calibration experiments, the error in the transducer's reading was about 1%, which represents the standard deviation of the data from a calibration curve obtained by utilizing the least-square-fit method. The piezoelectric sensor, which had a substantially higher resonant frequency, was used primarily to verify the shape of the pressure waveform. A 125 MHz Lecroy digital oscilloscope was used for recording the output of the transducer.

A special control system was constructed specifically for the present experiments. The controller provided the triggering pulses to the valve relays, the laser, the shutter, the film drive and the digital oscilloscope that recorded the transducer

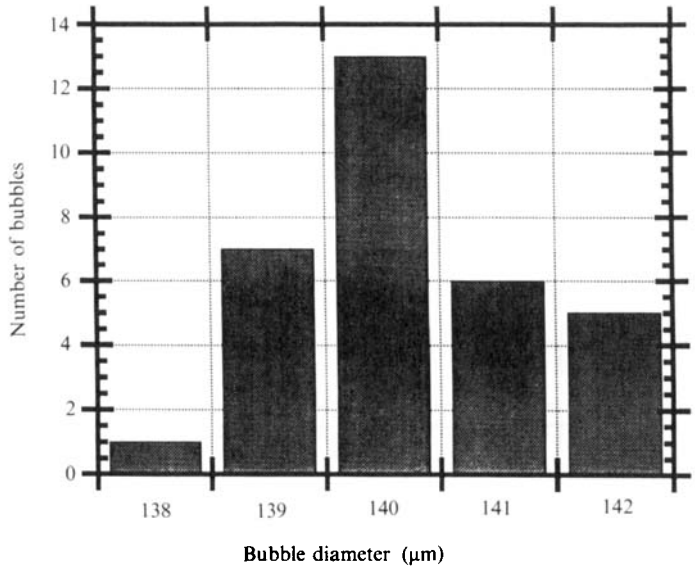

FIGURE 5. Size distribution of bubble diameters on a single hologram.

signal. A signal from the laser to the scope indicated the exact time of measurement, so the instantaneous pressure and the bubble size from the reconstructed hologram could be compared.

2.3. *Bubble injection*

The bubble injection system consisted of a regulator, a fine air filter, a fine metering valve, and a glass injector. The latter was made by stretching a glass capillary tube under heat until the external diameter of the exit diameter was reduced to less than 10 μm. Such a small nozzle was required since the bubbles were injected into still water, and only buoyancy could separate them from the nozzle's tip (as opposed to injection into a moving fluid, where shear stresses help in detaching the bubble). This set-up made it possible to generate a continuous train of uniform-size bubbles. A photograph of a train of 150 μm diameter bubbles rising above the injector is presented in figure 3. A sample reconstructed image of a single bubble of a similar size is provided in figure 4. Depending on the opening of the glass nozzle, as well as the pressure in the facility, the characteristic size of bubbles in the injected train varied between 90 and 400 μm in diameter. However, once the injection conditions had been carefully set by the fine metering valve, the injected bubbles maintained a uniform size. A typical sample size distribution of bubbles measured on the same hologram is presented in figure 5. The mean size of this sample is just above 140 μm and the variance is 1.114 mm. Note that the images were magnified by 500 times, and direct measurements on the TV screen had a typical error of 1 mm, namely an error of 2 μm in the actual bubble diameter. Thus, it seems that the variations in bubble size shown in figure 5 are of the same magnitude as our capability of resolving the bubble size. This consistency was examined and verified on each of the holograms recorded during the experiments, whether it was prior to or after changing the pressure. It should be noted here that algae growing on the nozzle (after few days in the water) as well as other contamination changed the size of the bubbles injected from the same nozzle. Frequent water replacement and careful filtering were used to overcome this problem.

In order to ensure that the undisturbed bubble size was known exactly, each

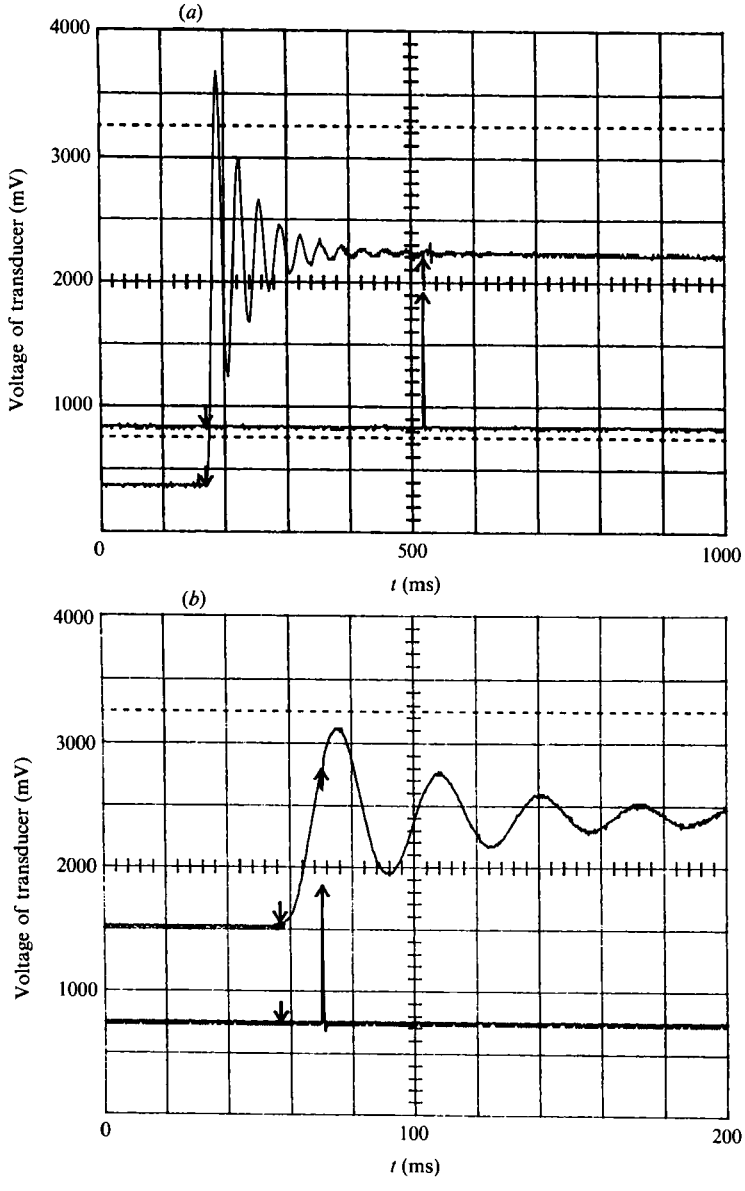

FIGURE 6. Pressure–time plots for a compression wave. These waveforms are typical of a set-up with a very small gas volume below the solenoid valve. (*a*) High-amplitude step; (*b*) initial stages of a low-amplitude step. (67.4 mV = 1 psi.)

experiment consisted of recording at least two holograms. The first one was recorded just prior to opening the solenoid valve, and the second was recorded while the pressure was changing. The distance between the injector and the sample volume was kept at about 15 cm. This distance ensured that the bubbles on the hologram were injected several seconds prior to changing the pressure. Since the rise time of a bubble due to buoyancy was 3–6 cm/s, depending on its size, it took the bubble 2.5–5 s to reach the sample volume. Since the timescales during the present measurements varied between less than 10 ms and 400 ms, this arrangement ensured that the hologram contains bubbles injected long before the pressure started changing.

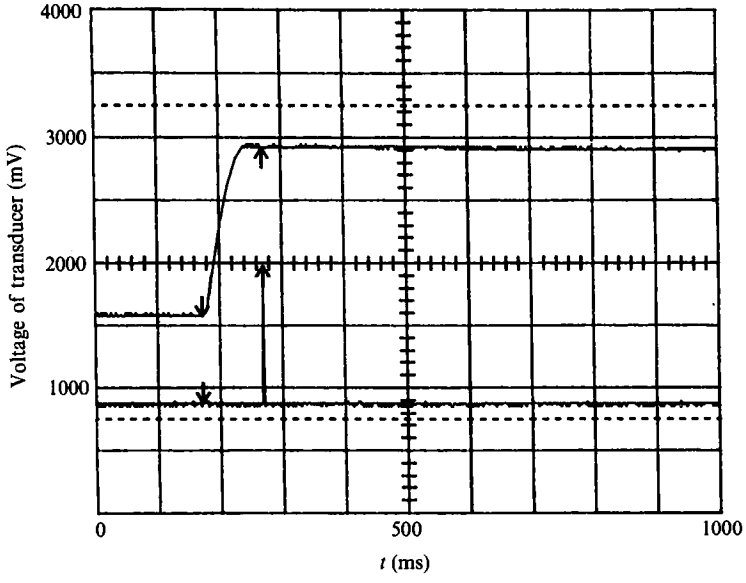

FIGURE 7. The pressure in the test section during a compression wave. This smooth transition occurs when the water level is lowered below the top of the main tank leaving a large gas volume below the valve.

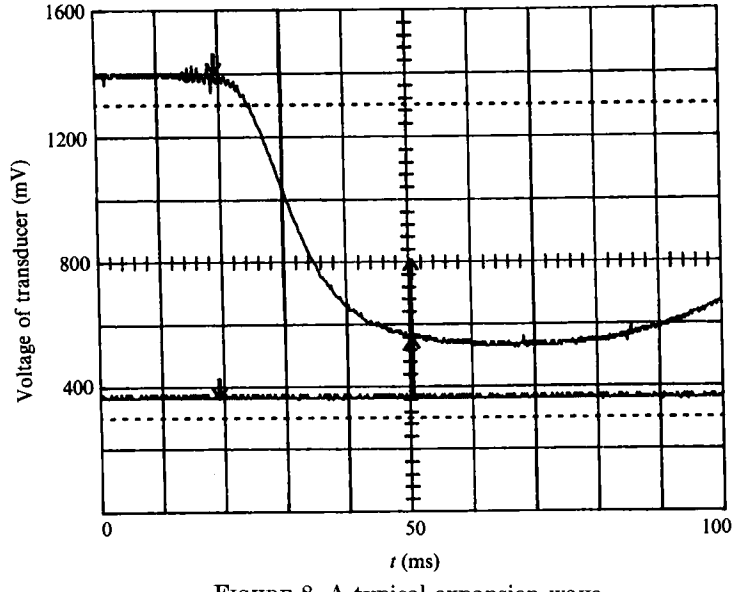

FIGURE 8. A typical expansion wave.

2.4. *Procedures*

At the beginning of an experiment the middle and upper chambers were pressurized to a prescribed value and a hologram of the bubble train was recorded. Then the solenoid valve was opened and at a prescribed delay a second hologram was recorded. The output of the transducers and the exact timing of the laser pulse were recorded by the digital oscilloscope. Typical pressure–time plots for a compression wave, specifying the laser timing (with an arrow) are presented in figure 6(*a*, *b*). Figure 6(*a*)

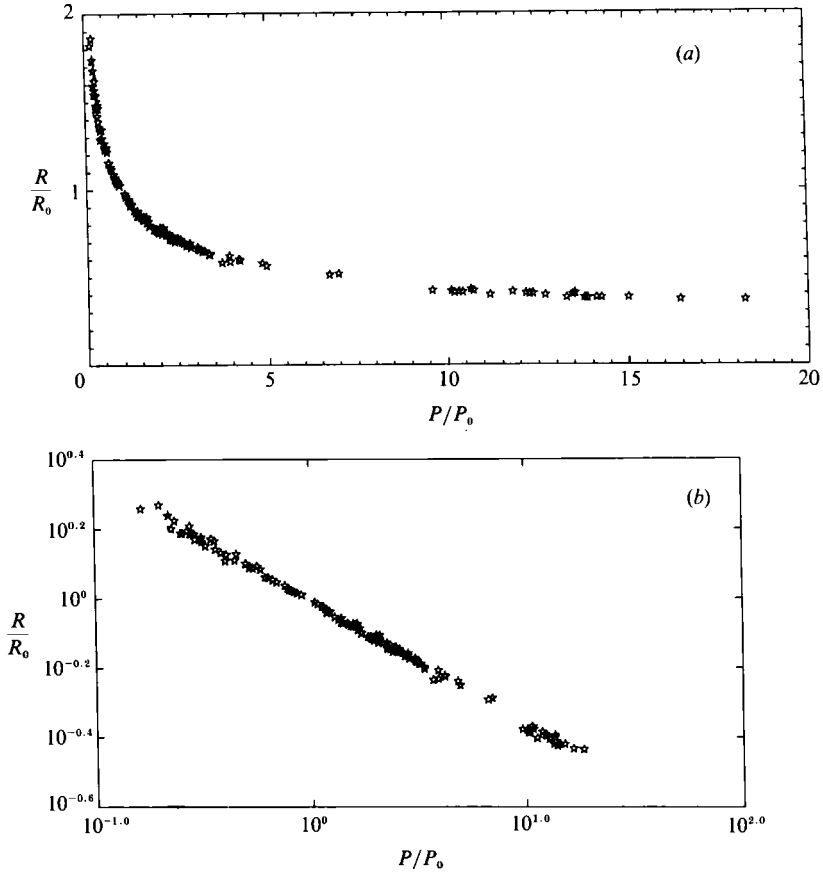

FIGURE 9. The response of air bubbles to changes in the ambient pressure plotted on both (*a*) linear; and (*b*) logarithmic scales. The subscript 0 indicates the initial conditions. Air content is 68%.

	Isentropic constant, γ	Thermal diffusivity, α (m^2/s)	Mass diffusivity, D (m^2/s)	Solubility in water (molar) atm, 25 °C (p.p.m.)
Air	1.4	0.22×10^{-4}	2.6×10^{-9}	13.9
Hydrogen	1.4	1.5×10^{-4}	5.85×10^{-9}	14.1
Helium	1.67	1.74×10^{-4}	3.4×10^{-9}	6.78
Carbon dioxide	1.33	0.1×10^{-4}	1.96×10^{-9}	610

TABLE 1. Properties of the gases used during the present study

shows a high-amplitude pressure step, and figure 6(*b*) contains the first 200 ms of a lower-amplitude wave. As is evident from this direct plot of the oscilloscope signal, pressure oscillations occurred during the initial phase of compression. This phenomenon appeared only when the water level was kept just below the top of the middle container, leaving a very small gas volume. Thus, transient pressures that are much higher than the initial levels in either tank could be obtained. The occurrence of these oscillations was verified by both transducers. The 'second-order behaviour' is probably a result of wave propagation through the valve separating the upper two

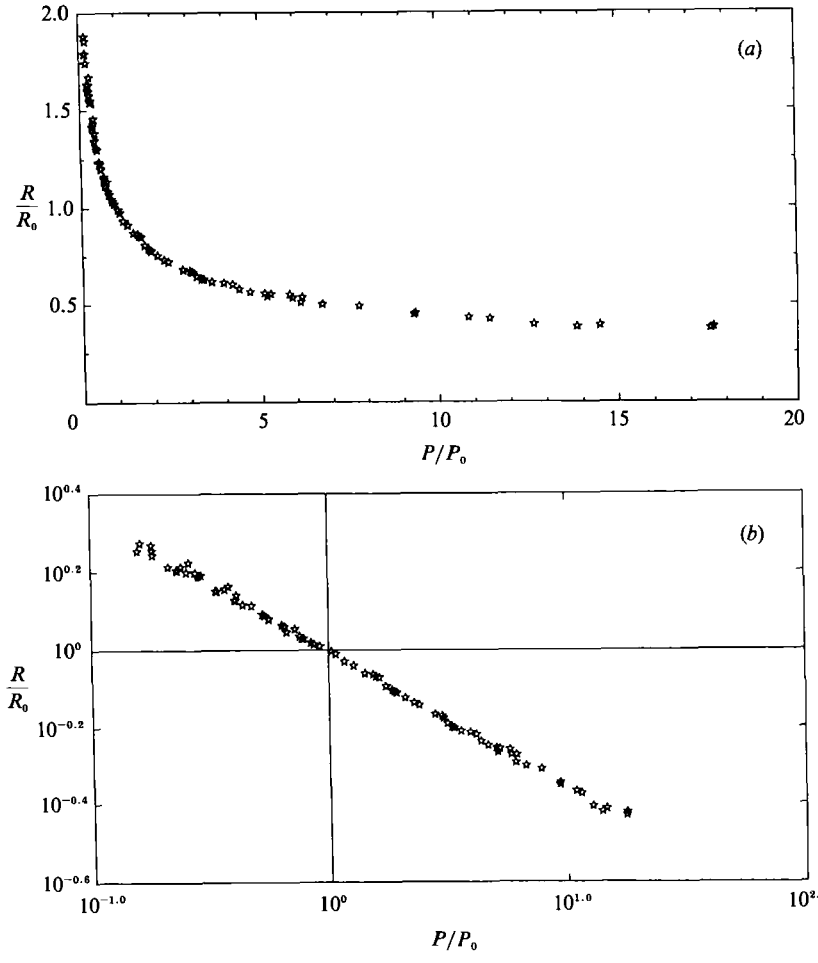

FIGURE 10. The response of hydrogen bubbles to changes in the ambient pressure.

chambers. One can utilize a simple model of a compressible flow through a tube and an orifice in order to explain these pressure oscillations. This model will probably include a choked flow during the initial stages, as well as a continued influx into the lower chamber that persists until the reflected wave propagating upward reaches the upper chamber. However, this phenomenon is not part of the scope of this study, and as a result will not be discussed further. Note that this behaviour enabled us to change the pressure by about 400 KPa in about 20 ms, namely 20 KPa/ms. The pressure oscillations disappeared when the water level was lowered below the top of the main test section, leaving as a result a substantially larger gas volume below the valve. A sample of the resulting pressure–time plot in the lower chamber is presented in figure 7. Finally, a typical expansion wave is presented in figure 8.

Four different gases were selected for the present study: hydrogen, air, helium, and carbon dioxide, since they represented a variety of thermal and mass diffusivities, and different isentropic exponents, and solubilities in water. Some essential properties of the selected gases are presented in table 1. As, noted before, some experiments, particularly those with air bubbles, were performed at different levels of dissolved gas. The water was dearated by keeping it under vacuum for extended

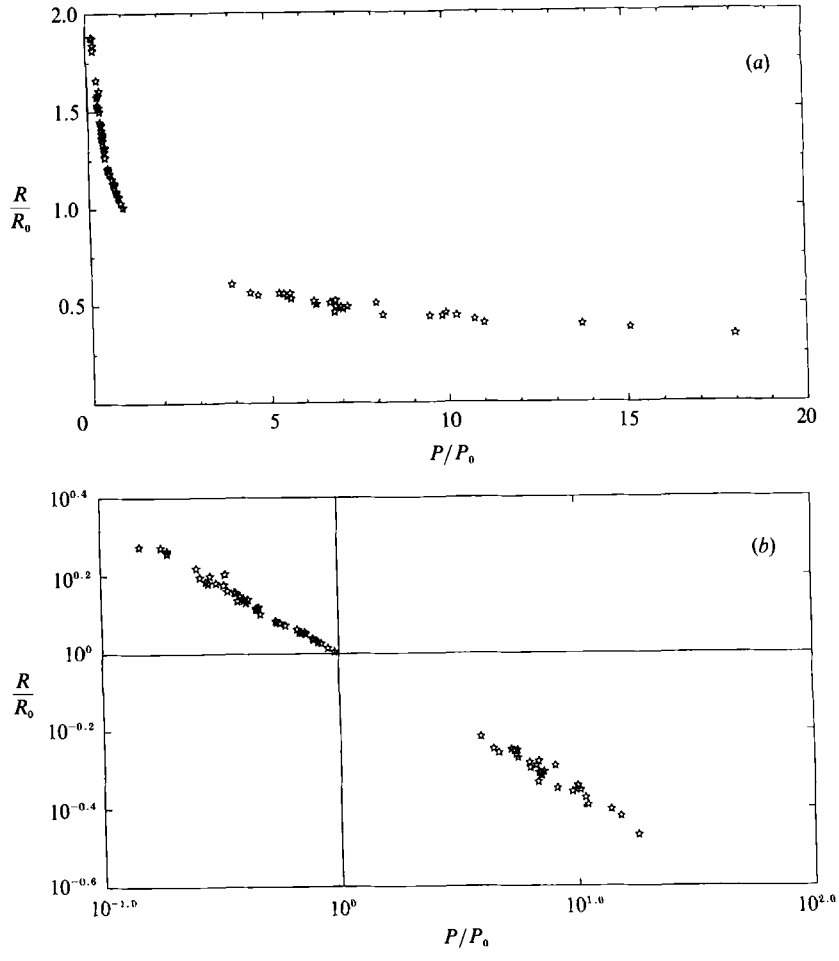

FIGURE 11. The response of helium bubbles to changes in the ambient pressure.

periods and the dissolved air content was evaluated with an oxygen meter. Repeated experiments with different levels of dissolved CO_2 were also performed. The results of these particular measurements were used for evaluating the effects of mass diffusion on the response of the bubbles.

3. Results

Figures 9–12 are a series of graphs containing the bulk of the data obtained during the present experiments. The results are presented as the ratio of the instantaneous and initial bubble radii, R/R_0, plotted against the ratio of the instantaneous and initial pressures, P/P_0. Note that P/P_0 extends between 0.2 and 20, namely the results for both compression and expansion waves. The bubbles have radii ranging between 45 to 200 μm and natural frequencies between 7.3 to 118 KHz. The actual values of P_0 extend between 24 KPa and 400 KPa. All the data presented in figures 9–12 represent the response of the bubbles during the initial pressure rise (or drop), namely prior to pressure oscillations (see figure 6). Thus, all the holograms included in these figures were recorded within less than 20 ms and a substantial number were actually recorded after less than 10 ms. Originally we planned to present the results

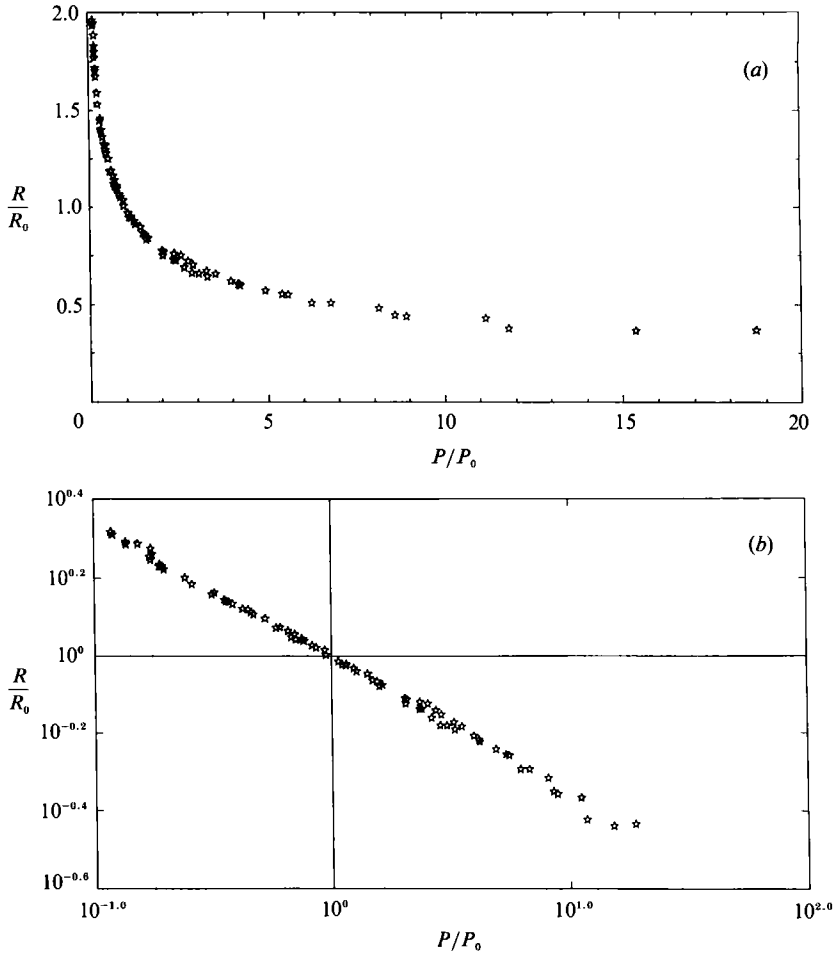

FIGURE 12. The response of CO_2 bubbles to changes in the ambient pressure.

for each condition separately. However, since the agreement between results obtained under substantially different initial conditions was better than the error in our measurements (see §5), all the information was merged together. As an example, table 2 provides the distribution of natural frequencies of the bubbles included in figure 9. The distributions for H_2, He, and CO_2 bubbles are similar although the actual numbers may be a little different.

Plotted on a logarithmic scale (see parts (*b*) of figures 9–12), the results display a clear power law. Furthermore, a comparison between the results presented in these figures clearly demonstrates that the same power law applies to all of them. The implication of these results will be discussed in the next section, concerned with computing the polytropic constants.

The effect of varying the timescales on the response of air bubbles is illustrated in figure 13. Three sets of data are included in this comparison. The first set is from figure 9 and represents data recorded in less than 20 ms. The other two sets represent much longer timescales, 90 and 400 ms, which were recorded with a 'smooth' pressure step, namely with a step similar to figure 7. Furthermore, they both represent the bubble response after the pressure in the facility settled to a constant

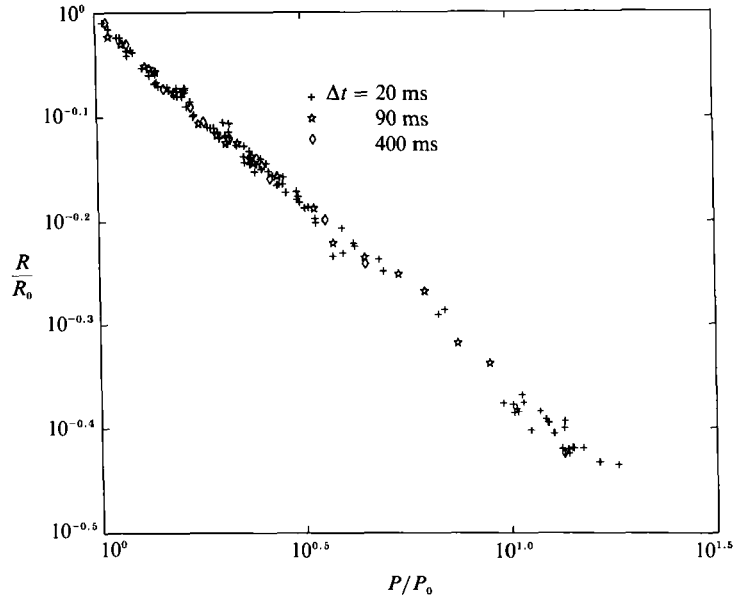

FIGURE 13. The effect of timescales on the response of air bubbles. The data at 90 and 400 ms represent exposure to a 'smooth' pressure step (see figure 7). The data at 20 ms refers to the initial rise prior to oscillations (figure 6).

ω_0, natural frequency (KHz)	Prior to experiment	Following experiment
5–10	23	5
10–15	—	13
15–20	1	12
20–30	15	13
30–40	101	4
40–50	4	19
50–60	3	19
60–80	1	36
> 80		27

TABLE 2. Distribution of natural frequencies of air bubbles used for plotting figure 9

value. This graph is important since it demonstrates that the response of the bubbles to pressure changes occurring in less than 20 ms is similar to their response after a substantially longer time. Rewriting (13) by replacing $1/\omega$ with the longest timescale of figure 13 one obtains

$$\left(\frac{R}{(\alpha t)^{\frac{1}{2}}}\right)_{\min} = 0.017 \tag{14a}$$

for a 50 μm radius air bubble. Thus, the thermal penetration distance, $(\alpha t)^{\frac{1}{2}}$ is much larger than the bubble radius, and as a result it should have ample time to reach thermal equilibrium. Figure 13 demonstrates clearly that the bubbles have already

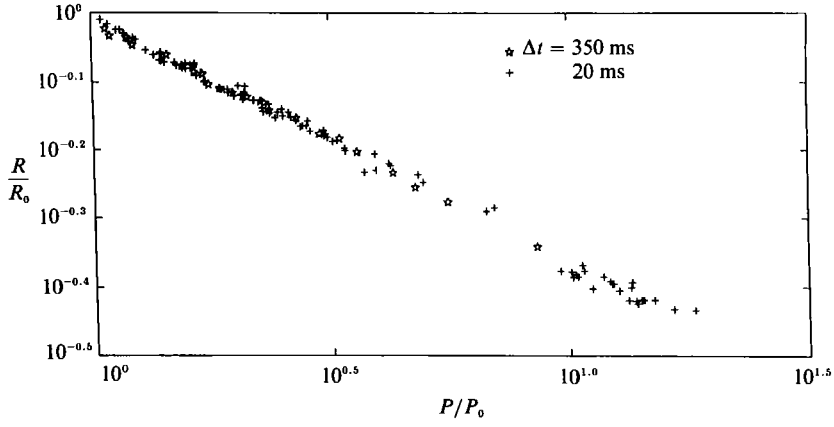

FIGURE 14. The effect of pressure–time history on the response of air bubbles. A comparison of the response during the initial pressure rise (20 ms) to the response following pressure oscillations (350 ms).

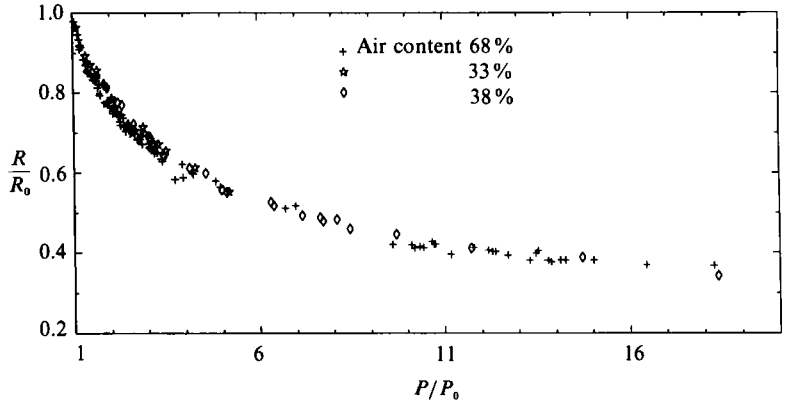

FIGURE 15. The effect of dissolved air content on the response of air bubbles.

reached thermal equilibrium, that is behave isothermally, in less than 20 ms. The highest ratio (between bubble radius and thermal penetration distance) during the present study is for a 200 μm radius CO_2 bubble and a 10 ms timestep. Thus

$$\left(\frac{R}{(\alpha t)^{\frac{1}{2}}}\right)_{\max} = 0.632. \tag{14b}$$

We shall return to this subject following the computations of the polytropic constants. Another comparison related to the possible use of bubbles as pressure sensors is presented in figure 14. It compares the response of bubbles during the initial pressure rise, namely prior to pressure oscillations, to their response long after the pressure has settled at a constant value. Again, there is no significant difference between the two sets of data. Thus, at least for the present range of test conditions, the bubble does not have a 'memory', namely it responds to the instantaneous pressure irrespective of its history.

The effect of dissolved air content on the response of air bubbles is presented in figure 15. The concentrations indicated on the graph refer to the percentage of the saturation level at atmospheric pressure. Logically one would expect that if mass

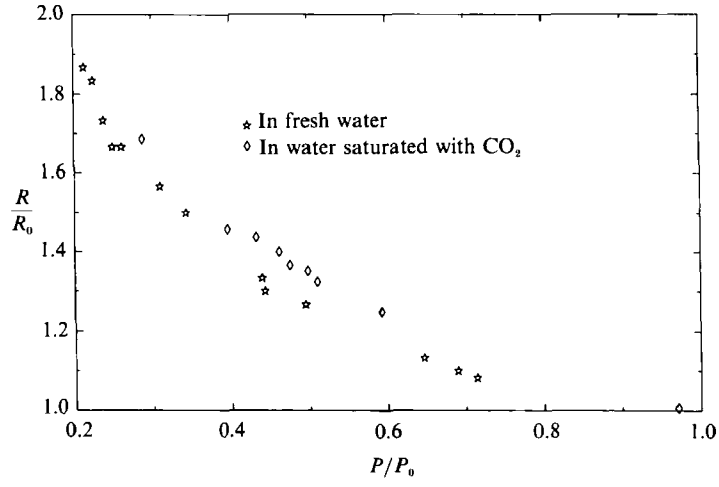

FIGURE 16. The effect of dissolved CO_2 content on the response of CO_2 bubbles.

diffusion has any significant effect on the results, the bubbles would dissolve faster when the dissolved gas concentration in the liquid is lower. Thus, a typical bubble should be smaller in a liquid with a lower concentration of dissolved air. Furthermore, longer timescales would increase the amount of mass transfer, also resulting in smaller bubbles. There is no evidence that either of these trends occurred during the present experiments with air bubbles. The slight difference observed in some data points is still within our error margin (see figure 18). This observation agrees with our previous assessment, namely that for the present timescales mass diffusion does not play an important role in the response of the air bubbles. A different conclusion is drawn from the CO_2 results presented in figure 16. This gas is the most soluble in water, although its diffusion coefficient is still very low. The experiments with saturated water were performed by injecting large quantities of CO_2 into the facility for extended periods of time. Then, the pressure was reduced slightly and very slowly until bubbles started appearing at various locations in the facility. It was assumed then that the water was saturated and the first hologram was recorded to determine R_0. As is evident from figure 16, the results for water saturated with CO_2 are higher than the bubble response at very low concentrations of dissolved gas. This result suggests that significant mass diffusion occurs during the experiment, resulting in a significant effect on the bubble size. It should be noted here that the experiments with water saturated with CO_2 were hard to control since even brief supersaturation, resulting from a brief reduction in the ambient pressure, resulted in the appearance of numerous bubbles all around the test chamber. This phenomenon is obviously familiar to anybody drinking soda.

4. The polytropic constant

The value of k, the polytropic constant, can be evaluated by reorganizing (12) as

$$k = \frac{1}{3}\frac{\ln\left[\dfrac{P+2\sigma/R-P_v}{P_0+2\sigma/R_0-P_{v0}}\right]}{\ln(R_0/R)}. \tag{15}$$

Thus, k can be estimated by replotting the present results as shown in figure 17 (a–d).

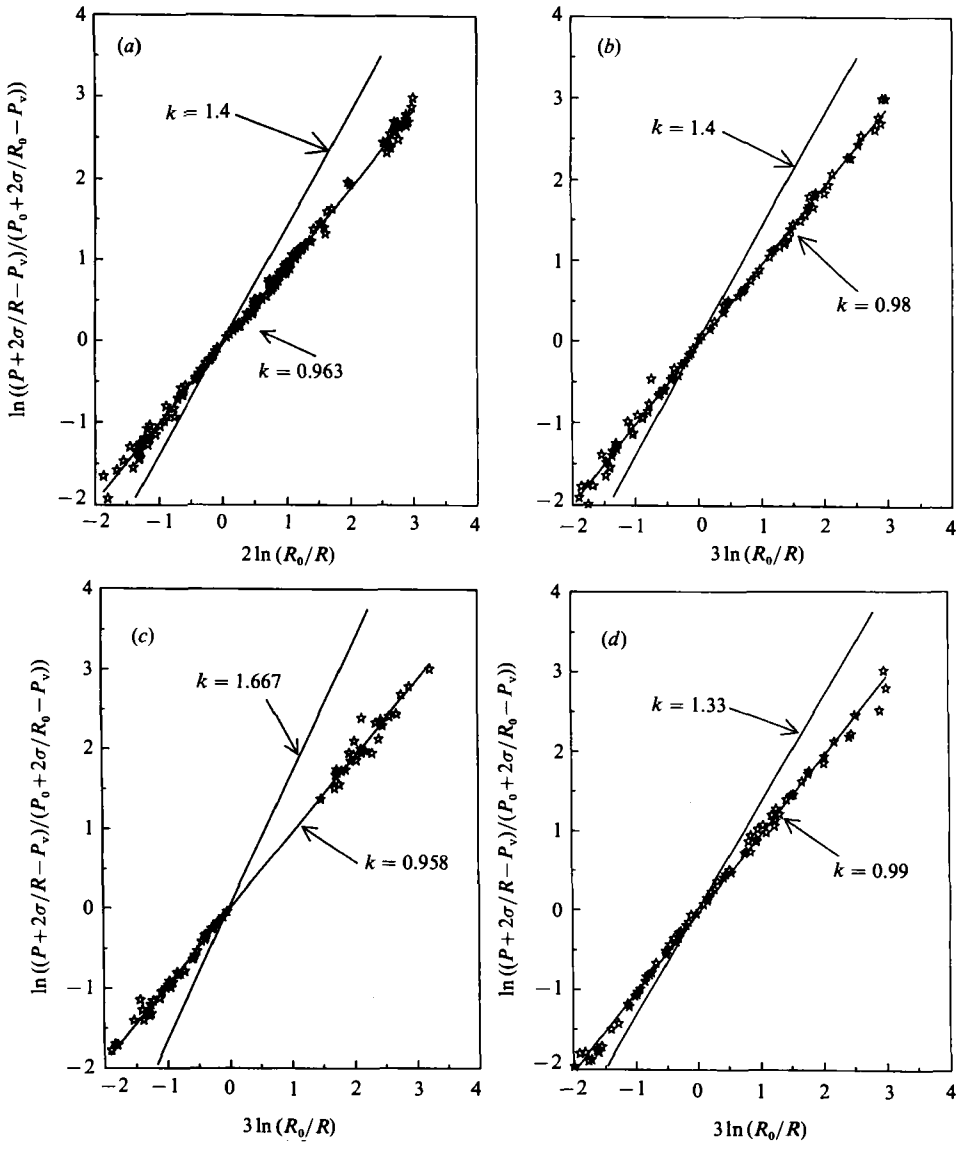

FIGURE 17. Determination of the polytropic constant for (*a*) air; (*b*) H_2; (*c*) He; (*d*) CO_2 bubbles.

The actual slopes indicated on each plot were calculated by a least-square-fit approximation. The resulting values of k were 0.96 for air and helium, 0.98 for hydrogen and 0.99 for CO_2. As will be discussed in detail in the following section, the estimated error in the value of k varies depending on the test conditions. However, for the majority of the present compression and expansion experiments this error is about 0.07. Thus, the differences between the polytropic constants obtained are smaller than the computed error, and one should not draw any conclusions from them. Actually, the present experiments have not identified any significant differences between the behaviour of the bubbles, irrespective of their sizes, natural frequencies, and type of gas within them. Note that these gases have isentropic constants varying between 1.33 and 1.67, and substantially different thermal diffusivities, (table 1) but yet the response of these bubbles is indistinguishable.

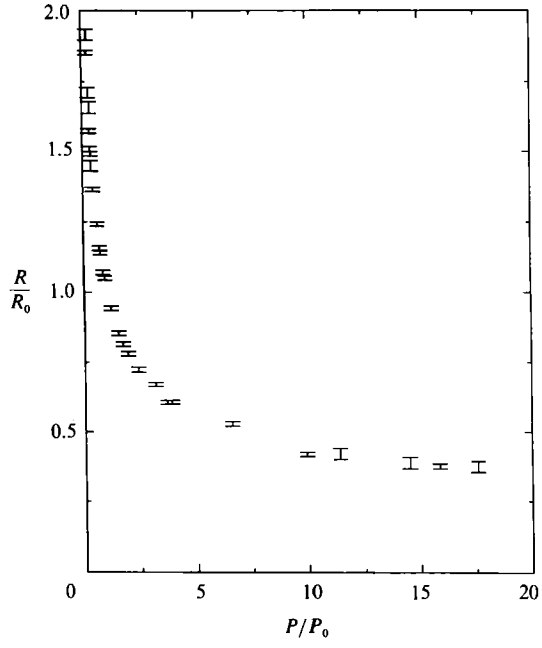

FIGURE 18. The results presented in figure 9, but with error bars replacing the original data. $\Delta(R/R_0) = 0.04$.

Furthermore, increasing the timescales by more than an order of magnitude (figure 13) does not cause any noticeable change. These trends lead to the clear conclusion that the response of the bubbles is isothermal. These results are also in agreement with the theoretical predictions which were discussed in the introduction. Thus, a polytropic constant of 1.0 should be used while utilizing bubbles as pressure sensors provided that one operates within the present envelope of test conditions. As far as thermal effects are concerned, this envelope is identified in (14*b*). By utilizing a 50 μm radius helium bubble, for example, the timescale (R^2/α) is reduced to 0.036 ms. If we replace this number with $1/\omega$, the value of ω is of the order of 28000 rad/s. Similar sized air bubbles result in a timescale of 0.28 ms. Thus, with a proper choice of gas, the present experiments provide sufficient operating range for measurements within turbulent flows.

5. Error analysis

This section contains two parts, the first dealing with the error in the present measurements, and the second providing an estimate of the accuracy of pressure measurements with bubbles as pressure sensors. Only summarized results are presented. Detailed derivations of the various expressions presented are given in the Appendix.

5.1. *Present measurements*

A sample plot containing error bars for the values of R/R_0 is presented in figure 18. The length of these bars is estimated from the following expression:

$$\Delta\left(\frac{R}{R_0}\right) = \left[\left(\frac{1}{R_0}\Delta R\right)^2 + \left(\frac{R}{R_0^2}\Delta R_0\right)^2\right]^{\frac{1}{2}}. \tag{16}$$

$\frac{R_0}{R}$	$\frac{P_0}{P}$	Δk
0.5	8	0.05
0.6	4.63	0.055
0.7	2.92	0.074
0.8	1.95	0.1194
1.0	1	∞
1.1	0.75	0.312
1.3	0.455	0.125
1.5	0.296	0.090
1.8	0.17	0.070
2.0	0.125	0.064
2.5	0.064	0.059

TABLE 3. Calculated values of Δk, the error in the polytropic constant, for typical bubble size ratios. $\Delta R/R_0 = 0.02$, $\Delta P/P_0 = 0.01$

As noted before, the error in measuring the bubble diameter directly from the TV screen is about 2 μm namely the value of ΔR is 1 μm. Owing to variations in the actual values of R and R_0, the lengths of these error bars vary significantly. A typical value of this error varies between 1.1 and 2.0 times $\Delta R/R_0$, that is between 2% and 4% for a 50 μm radius bubble, and about half this value for a 100 μm radius bubble.

More important, however, is the error in our estimates for the polytropic constant. It can be evaluated first by determining the 'scatter' (standard deviation) of the data plotted in figure 17 (*a–d*) around the computed line. These standard deviations are 0.082, 0.086, 0.094 and 0.099 for air, hydrogen, helium and carbon dioxide, respectively. Thus, the respective standard deviations of the slopes (computed from the data standard deviations) are 0.005, 0.0067, 0.0071 and 0.008. However, the actual value of Δk should be evaluated by using (15). Based on derivations and simplifications described in the Appendix an estimated expression for Δk is

$$\Delta k \approx \frac{1}{|3\ln(R_0/R)|}\left\{\frac{(3k\Delta R)^2}{R_0^2}\left[1+\left(\frac{R_0}{R}\right)^2\right]+\frac{(\Delta P)^2}{(P_0)^2}\left[1+\left(\frac{P_0}{P}\right)^2\right]\right\}^{\frac{1}{2}}. \tag{17}$$

A few typical values that cover the present range of test conditions are presented in table 3. Selecting a specific value for future analysis is somewhat arbitrary, and depends on how conservative one would like to be. Note also that the standard deviation of k, which is computed from the data presented in figure 17 (*a–d*), agrees with the results presented in table 3. A relatively conservative value of 0.07, which covers most of the present test conditions, has been selected. Thus,

$$\left.\begin{aligned} k_{\text{air}} &= 0.96 \pm 0.07, \\ k_{\text{helium}} &= 0.96 \pm 0.07, \\ k_{\text{hydrogen}} &= 0.98 \pm 0.07, \\ k_{\text{CO}_2} &= 0.99 \pm 0.07. \end{aligned}\right\} \tag{18}$$

As stated before, (18) and the apparent insensitivity of the bubble response to substantial changes in the timescales (figures 13 and 14) clearly demonstrate that the bubbles behave isothermally. Thus, one can assume that k is equal to 1.0 provided that one operates within the present test conditions.

$\frac{\Delta R}{R_0}$	V (m/s)	$\frac{1}{2}\rho v^2$ (KPa)	P_0 (KPa)	P (KPa)	$\frac{R}{R_0}$	$\frac{\Delta P}{P}$	$\frac{\Delta P}{P'}$
0.02	10	50	100	150	0.87	0.080	0.24
0.02	10	50	100	50	1.26	0.097	0.097
0.02	20	200	300	500	0.84	0.079	0.20
0.02	20	200	300	100	1.44	0.105	0.053

TABLE 4. Estimated values of ΔP computed from (19)

5.2. *Future measurements*

The next step is evaluation of the error while utilizing microscopic bubbles as pressure sensors. Based on the derivation and simplifications provided in the Appendix, ΔP can be estimated as

$$\left.\begin{aligned} \Delta P &\approx 3kP\frac{\Delta R_0}{R_0}\left[1+\left(\frac{R_0}{R}\right)^2\right]^{\frac{1}{2}} \\ \text{or}\quad \Delta P &\approx 3kP\frac{\Delta R}{R}\left[1+\left(\frac{R}{R_0}\right)^2\right]^{\frac{1}{2}}. \end{aligned}\right\} \tag{19}$$

By substituting $\Delta R/R \approx 0.02$ and $k = 1$, in (19) the estimated expression for ΔP becomes

$$\frac{\Delta P}{P} \approx 0.06\left[1+\left(\frac{R}{R_0}\right)^2\right]^{\frac{1}{2}}. \tag{20}$$

Improvements in this error can be achieved by measuring the bubble's cross-sectional area A instead of its radius. Then, since $\Delta R/R = \frac{1}{2}\Delta A/A$ and $(R/R_0)^2 = A/A_0$ the error becomes

$$\frac{\Delta P}{P} \approx \tfrac{3}{2}k\frac{\Delta A}{A}\left[1+\frac{A}{A_0}\right]^{\frac{1}{2}}. \tag{21}$$

We shall attempt to utilize this approach in the future, by digitizing the image of the bubble and measuring its area by counting image pixels. If the error in evaluating the area is kept similar to the error in measuring the radius (a reasonable assumption provided special care is used), then ΔP can be reduced by 50 %.

Finally, let us try to determine the impact of the error on pressure measurements within turbulent flows. The results of Ooi & Acosta (1983) and O'Hern (1987) within turbulent jets and wakes, respectively show that pressure fluctuations exist with amplitudes comparable with the dynamic head ($0.5\,\mathrm{pv}^2$, where V is a characteristic velocity). This result can be utilized for estimating P, the instantaneous pressure. Several computed values for ΔP (based on (19)), at two different velocities are summarized in table 4. Note that P_0 at 20 m/s is higher in order to prevent conditions that are favourable for inception of cavitation. This table demonstrates that errors of less than 10 % are possible, but care should be used while selecting the test conditions. As noted before, area instead of radius measurements will reduce this error by 50 %.

6. Conclusions

The results described in this paper confirm that, within the present range of test conditions, the bubbles can reach dynamic equilibrium with the ambient pressure. These results are in agreement with theoretical evaluations. The experiments also demonstrate that the response of the bubbles at the present timescales can be assumed to be isothermal (polytropic constant of 1.0), irrespective of the bubble content or size. Repeated measurements with different pressure waveforms, but with the same final pressure resulted in identical results, demonstrating that bubbles can be used as pressure sensors. Variations in timescales up to a few hundred milliseconds still resulted in the same response, confirming the assumption of isothermal response. The dissolve gas content had a noticeable effect on the behaviour of the CO_2 bubbles, the most soluble of the gases tested, and had no detectable effect on the behaviour of air bubbles. The latter conclusion is also supported by the agreement between results recorded in less than 20 ms and after 400 ms.

This research project was supported by The National Science Foundation under Grant no. MSM-851065. The ruby laser holocamera was purchased with an NSF Engineering Research Equipment Grant no. MSM-8705120. The authors would like to express their gratitude for this support. We would also like to acknowledge the technical assistance of Van Hooijdonk, John Woomer and Curt Ewing, as well as the contribution of Ronald Dong to the construction of the electronic control system.

Appendix. Error estimates

The value of Δk can be estimated from (15) and that

$$\Delta k = \left[\left(\frac{\partial k}{\partial R}\Delta R\right)^2 + \left(\frac{\partial k}{\partial R_0}\Delta R_0\right)^2 + \left(\frac{\partial k}{\partial P}\Delta P\right)^2 + \left(\frac{\partial k}{\partial P_0}\Delta P_0\right)^2\right]^{\frac{1}{2}} \tag{A 1}$$

where

$$\frac{\partial k}{\partial R} = \frac{1}{3R\ln\left(\frac{R_0}{R}\right)}\left[\frac{-2\sigma/R}{\left(P+\frac{2\sigma}{R}-P_v\right)}+3k\right], \tag{A 2}$$

$$\frac{\partial k}{\partial R_0} = \frac{1}{3R_0\ln\left(\frac{R_0}{R}\right)}\left[\frac{2\sigma/R_0}{\left(P_0+\frac{2\sigma}{R_0}-P_v\right)}-3k\right], \tag{A 3}$$

$$\frac{\partial k}{\partial P} = \frac{1}{2\ln\left(\frac{R_0}{R}\right)\left(P+\frac{2\sigma}{R}-P_v\right)} \tag{A 4}$$

and finally

$$\frac{\partial k}{\partial P_0} = \frac{-1}{3\ln\left(\frac{R_0}{R}\right)\left(P_0+\frac{2\sigma}{R_0}-P_v\right)}. \tag{A 5}$$

Since the terms containing the surface tension in (A 2)–(A 3) are very small, they can be neglected. Furthermore, $2\sigma/R$ and P_v in (A 4) and (A 5) are much smaller than P or P_0 and can also be neglected. Thus, the error in k can be estimated as

$$\Delta k \approx \frac{1}{|3\ln(R_0/R)|}\left\{\frac{(3k\Delta R)^2}{R_0^2}\left[1+\left(\frac{R_0}{R}\right)^2\right]+\frac{(\Delta P)^2}{(P_0)^2}\left[1+\left(\frac{P_0}{P}\right)^2\right]\right\}^{\frac{1}{2}}. \tag{A 6}$$

Further details are discussed in the main text.

The next step is evaluation of the error while utilizing microscopic bubbles as pressure sensors. Based on (12), such a technique involves measurements of R, R_0 and P_0. Thus, an estimate for the error should be in the form

$$\Delta P = \left[\left(\frac{\partial P}{\partial P_0}\Delta P_0\right)^2 + \left(\frac{\partial P}{\partial R}\Delta R\right)^2 + \left(\frac{\partial P}{\partial R_0}\Delta R_0\right)^2\right]^{\frac{1}{2}}, \tag{A 7}$$

where

$$\frac{\partial P}{\partial R} = -\frac{3k}{R}\left(P_0 + \frac{2\sigma}{R_0} - P_{v0}\right)\left(\frac{R_0}{R}\right)^{3k} + \frac{2\sigma}{R^2}, \tag{A 8}$$

$$\frac{\partial P}{\partial R_0} = \frac{3k}{R_0}\left(P_0 + \frac{2\sigma}{R_0} - P_{v0}\right)\left(\frac{R_0}{R}\right)^{3k} - \left(\frac{R_0}{R}\right)^{3k}\frac{2\sigma}{R_0^2}, \tag{A 9}$$

$$\frac{\partial P}{\partial P_0} = \left(\frac{R_0}{R}\right)^{3k}. \tag{A 10}$$

Simplifying these expressions by neglecting the surface tension and vapour pressure compared to P or P_0 results in the following estimate for the error:

$$\Delta P \approx \left(\frac{R_0}{R}\right)^{3k}\left\{\left[\frac{3kP_0}{R_0}\Delta R_0\right]^2 + \left[\frac{3kP_0}{R}\Delta R\right]^2 + [\Delta P_0]^2\right\}^{\frac{1}{2}}. \tag{A 11}$$

The third term in this expression is much smaller than the first two (assuming that the accuracy in measuring P_0, the steady initial pressure where the bubble is generated, is reasonable), and as a result we can simplify (A 11) and express ΔP as

$$\Delta P \approx \left(\frac{R_0}{R}\right)^{3k}\frac{3kP_0}{R_0}\Delta R_0\left[1 + \left(\frac{R_0}{R}\right)^2\right]^{\frac{1}{2}}. \tag{A 12}$$

Note also that, in the context of error evaluation, and by utilizing the same assumptions used for obtaining (A 11), we can substitute

$$\left(\frac{R_0}{R}\right)^{3k} \approx \frac{P}{P_0}; \tag{A 13}$$

then

$$\left.\begin{aligned} \Delta P &\approx 3kP\frac{\Delta R_0}{R_0}\left[1 + \left(\frac{R_0}{R}\right)^2\right]^{\frac{1}{2}} \\ \text{or} \quad \Delta P &\approx 3kP\frac{\Delta R}{R}\left[1 + \left(\frac{R}{R_0}\right)^2\right]^{\frac{1}{2}}. \end{aligned}\right\} \tag{A 14}$$

REFERENCES

Arndt, R. E. A. 1981 Cavitation in fluid machinery and hydraulic structures. *Ann. Rev. Fluid Mech.* **13**, 273–328.

Arndt, R. E. A. & George, W. K. 1978 Pressure fields and cavitation in turbulent shear flows. In *12th Symp. on Naval Hydrodynamics, Washington DC*, pp. 327–339.

Collier, R. J., Burkhardt, C. B. & Lin, L. H. 1970 *Optical Holography*. Academic.

Crum, L. A. 1983 The polytropic exponent of gas contained within air bubbles pulsating in a liquid. *J. Acoust. Soc. Am.* **73**, 116–120.

Fuchs, H. V. 1972 Measurements of pressure fluctuations within subsonic turbulent jets. *J. Sound Vib.* **22**, 361–378.

GREEN, S. I. 1988 Tip vortices – single phase and cavitating flow phenomena. Ph.D. thesis, California Institute of Technology; *Rep. No.* Eng. 183–17.

HSIEH, D. Y. & PLESSET, M. S. 1961 Theory of rectified diffusion of mass into gas bubbles. *J. Acoust. Soc. Am.* **33**, 206–215, February.

HUSSAIN, A. K. M. F. 1986 Coherent structures and turbulence. *J. Fluid Mech.* **173**, 303–356.

KELLER, J. B. & MIKSIS, M. 1980 Bubble oscillations of large amplitude. *J. Acoust. Soc. Am.* **68**, 628–633.

O'HERN, T. J. 1987 Cavitation inception scale effects: I. Nuclei distributions in natural waters; II. Cavitation inception in turbulent shear flow. Ph.D. thesis, California Institute of Technology; *Rep. No.* 183–15.

OOI, K. K. & ACOSTA, A. J. 1983 The utilization of specially tailored air bubbles as static pressure sensors in a jet. *Trans. ASME* I: *J. Fluids Engng* **106**, No. 4, pp. 459–465.

PLESSET, M. S. & PROSPERETTI, A. P. 1977 Bubble dynamics and cavitation. *Ann. Rev. Fluid Mech.* **9**, 145–185.

PROSPERETTI, A. P. 1977 Thermal effects and damping mechanisms in the forced radial oscillations of gas bubbles in liquids. *J. Acoust. Soc. Am.* **61**, 17–27.

PROSPERETTI, A. P. 1984 Bubble phenomena in sound fields: Part two. *Ultrasonics* **22**, 69–77.

PROSPERETTI, A. P., CRUM, L. A. & COMMANDER, K. W. 1988 Nonlinear bubble dynamics. *J. Acoust. Soc. Am.* **83**, 502–514.